Journal of Alloys and Compounds 639 (2015) 488–495

Contents lists available at ScienceDirect

Journal of Alloys and Compounds

journal homepage: www.elsevier.com/locate/jalcom

Co-sputtered amorphous Nb–Ta, Nb–Zr and Ta–Zr coatings for corrosion protection of cyclotron targets for [^{18}F] production

Hanna Skliarova [a,b,*], Oscar Azzolini [a], Richard R. Johnson [c], Vincenzo Palmieri [a,d]

[a] National Institute of Nuclear Physics, Legnaro National Laboratories, Viale dell'Università, 2, 35020 Legnaro, Padua, Italy
[b] University of Ferrara, Ferrara, Italy
[c] BEST Cyclotron Systems Inc., 8765 Ash Street Unit 7, Vancouver, BC V6P 6T3, Canada
[d] University of Padua, Padua, Italy

ARTICLE INFO

Article history:
Received 17 December 2014
Received in revised form 5 March 2015
Accepted 23 March 2015
Available online 28 March 2015

Keywords:
Magnetron sputtering
Thin films
Diffusion barrier
X-ray diffraction
Microstructure
Metallic glasses

ABSTRACT

Protective corrosion resistant coatings serve for decreasing the amount of ionic contaminants from Havar® entrance foils of the targets for [^{18}F] production. The corrosion damage of coated entrance foils is caused mainly by the diffusion of highly reactive products of water radiolysis through the protective film toward Havar® substrate. Since amorphous metal alloys (metallic glasses) are well-known to perform a high corrosion resistance, the glass forming ability, microstructure and diffusion barrier efficiency of binary alloys containing chemically inert Nb, Ta, Zr were investigated. Nb–Ta, Nb–Zr and Ta–Zr films of different alloy composition and ~1.5 μm thickness were co-deposited by magnetron sputtering. Diffusion barrier efficiency tests used reactive aluminum underlayer and protons of acid solution and gallium atoms at elevated temperature as diffusing particles. Though co-sputtered Nb–Ta and Nb–Zr alloy films of different contents were crystalline, Ta–Zr alloy was found to form dense amorphous microstructures in a range of composition with 30–73% atomic Ta. The diffusion barrier efficiency of Nb–Zr and Nb–Ta alloy coatings decreased with increase of Nb content. The diffusion barrier efficiency of sputtered Ta–Zr alloy coatings increased with the transition from nanocrystalline columnar microstructure to amorphous for coatings with 30–73 at.% Ta.

1. Introduction

The number of medical procedures involving the use of cyclotron-produced radionuclides is constantly growing year by year. [^{18}F]Fluoro-2-deoxy-D-glucose ([^{18}F]FDG), an analogue of glucose that is labeled with [^{18}F], makes up the large majority of all of the radiotracer (>95%) used in PET (Positron Emission Tomography) and PET/CT scanning. FDG is produced typically by proton irradiation of enriched water targets in an 18 MeV proton cyclotron. Water becomes an extremely corrosive media because of a number of highly reactive species occurring during proton irradiation. It shortens a lot the life time of Havar® entrance foils usually used for [^{18}F] production and initiate a large amount of ionic contaminants from Havar® [1,2].

When designing the cyclotron target for [^{18}F] production it is not always possible to find the material that corresponds simultaneously to all mechanical and physicochemical requirements. The use of thermally and mechanically suitable substrate materials, like Havar®, protected by chemical resistant coating was found to be a compromise. It was proven that the use of sputtered niobium coating on Havar® entrance foils decreases the amount of ionic long-lived impurities during [^{18}F] production more than ten times [3]. The next experiments in the area showed an even higher performance of tantalum protective coatings [4].

From the corrosion point of view, the combination of elements, which are able to maintain the passive state in a given environment, is the principle of protective coating design. For passive films the ability as the diffusion barrier appears to be also extremely important characteristic. For crystalline films, the grain boundaries tend to act as the main diffusion path for ions to penetrate through the barrier layer. However, amorphous alloys (also called metallic glasses), which normally have the dense and boundary-free structure, are known to eliminate effectively the fast diffusion paths [5], resulting in several cases even higher corrosion protection efficiency than single metals [6–8]. In a range of corrosion conditions,

* Corresponding author at: National Institute of Nuclear Physics, Legnaro National Laboratories, Viale dell'Università, 2 – 35020 Legnaro, Padua, Italy. Tel.: +39 3201837213.
E-mail addresses: Hanna.Skliarova@lnl.infn.it (H. Skliarova), Oscar.Azzolini@lnl.infn.it (O. Azzolini), richard.johnson@teambest.com (R.R. Johnson), Vincenzo.Palmieri@lnl.infn.it (V. Palmieri).

http://dx.doi.org/10.1016/j.jallcom.2015.03.181
0925-8388/

amorphous metallic glass systems have shown higher corrosion resistance than crystallized ones with equal compositions [9,10]. Besides that amorphous metallic glasses were shown to resist to irradiation [11,12] even improving plasticity while crystalline metals degrade fast, that is important feature for the nuclear application.

In order to improve corrosion protection efficiency of cyclotron target Havar® entrance foils we applied the idea of amorphous protective coating. Three elements, niobium, tantalum and zirconium, were chosen in current investigation as candidates for binary alloy protective coatings because of extreme chemical stability of single metals [13] as well as their alloy combinations [14–16] and because of small amount of radionuclide impurities that can be produced during irradiation and appear in the final radiopharmaceutical product [1].

The general procedure for the synthesis of metallic glasses is to "energize" and then "quench" the material. This can be done by a variety of methods: conventional quenching [17], different mechanical cold working [18], evaporation [19], sputtering [20–23], ion implantation and electron irradiation, annealing induced solid-state amorphization of multilayered films [24–26].

For immiscible systems (characterized by positive heat of formation), such as Nb–Zr, Nb–Ta and Ta–Zr, the occurrence of amorphous structures is provided under non-equilibrium conditions. Thus the glass forming ability (GFA) can be improved and the amorphization ranges are wider when metallic alloy coating is formed by non-equilibrium processes as sputtering [27,28] or ion beam mixing. Hereby amorphous Ta–Zr alloy coatings were prepared by ion beam mixing [29], co-condensation [30] and co-sputtering [31,32]. Formation of Ta-rich amorphous phases by high current pulse electron beam melting of Nb–Ta multilayers was mentioned [33]. Amorphous Nb–Zr coatings were prepared by sputtering onto liquid nitrogen cooled substrate [34] and by ion-beam mixing of multilayers [34–37]. Although amorphous Ta–Zr and Nb–Zr alloy coatings were successfully prepared by co-sputtering, amorphization ranges vary depending on the deposition parameters and should be controlled in each specific case. No attempts to produce amorphous Nb–Ta alloy coatings by co-sputtering were reported. Extensive studies were focused on glass formation and physical properties of alloys. The data on their performance as diffusion barriers are limited by study of Ta–Zr as diffusion barrier for copper at high temperature [31].

The objective of the current work was to determine the possibilities to obtain amorphous binary alloy coatings by co-sputtering of chosen refractory metals (niobium, nantalum and zirconium) and the impact of amorphization on the barrier properties of the coatings in order to find best protective coating for cyclotron target entrance foils. The use of an appropriate protective coating can drastically decrease the amount of long-lived impurities during [^{18}F] production and thus increase the labeling yield and the specific activity of the final radiopharmaceutical [^{18}F]FDG.

2. Materials and methods

2.1. Sputtering

The alloys were deposited by DC magnetron co-sputtering with two 2 in. in diameter planar cathode unbalanced magnetron sources (II type in the Window and Savvides classification [38]) in a cylindrical, 316 L stainless steel vacuum chamber of 35 cm diameter and 40 cm in length. Before sputtering, the chamber was initially pumped to a base pressure of $3{\cdot}10^{-6}$ mbar. The sample holder with 10 different fixed positions (Fig. 1) allowed to obtain samples with different alloy contents simultaneously. The sample holder during deposition was grounded without heating or cooling. 10 cm target-sample holder distance was chosen for optimal uniformity of coating thickness in different positions. 0.5 A DC-current was used for each magnetron source during alloys co-sputtering.

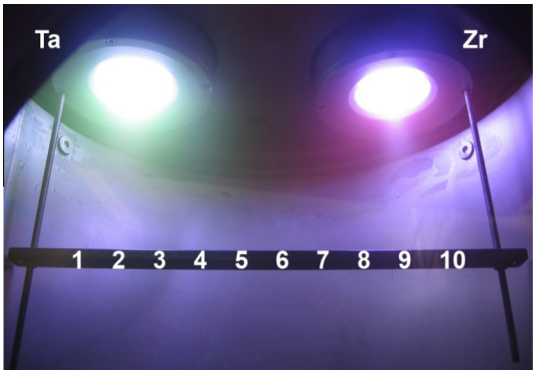

Fig. 1. Ta–Zr deposition. Sample holder for alloy co-sputtering.

Niobium, zirconium and tantalum targets with purity 99.9%, 99.2% and 99.9% respectively and argon (99.9999% purity) as process gas were used for alloys deposition.

Tensile stress in a metallic thin film signifies a voided film structure with a big distance between the grain boundaries. On the other hand, high compressive stress can cause film delamination from the substrate. Both cases are detrimental for corrosion protective films. Furthermore, presence of both tensile and compressive stress can induce crystallization of metallic glasses [39–41]. Therefore, minimization of the residual stress in the coatings is required. It is well known that the intrinsic stress in sputtered films drastically depends on a sputtering gas pressure. There is a specific sputtering pressure for each combination of a sputtered material and deposition system, at which stress reversal from compressive to tensile stress occurs. In order to find the optimal pressure for alloy co-sputtering, which means with minimal intrinsic stress in films, a deposition onto a flexible substrate (Kapton) was performed as described by Entenberg and coauthors [42]. Two types of stress can be observed: tensile, in which the film is trying to contract on the substrate and compressive, in which the film is trying to expand on the substrate. The intrinsic stress can be estimated directly from the radius of curvature of the relaxed film and substrate.

The flexible substrates have been placed in three positions on the sample holder: positions 2, 9 and between 5 and 6 – in the center (Fig. 1). Change of a radius of curvature of the coated flexible substrate from negative to positive identifies the transition from compressive to tensile stress. Each material has its own pressure of the compressive-tensile stress conversion. Co-sputtering involving two materials is more difficult, so we have considered optimal the pressure corresponding to the stress conversion along the sample holder (mostly in the center of SH). In this case, the total stress in all alloy films is minimal. Thus the Ar working pressure $5{\cdot}10^{-3}$ - mbar was chosen for Nb–Zr co-deposition, $7{\cdot}10^{-3}$ mbar for Nb–Ta and $8{\cdot}10^{-3}$ mbar for Ta–Zr co-deposition.

2.2. Estimation of diffusion barrier efficiency

The irradiation models for water radiolysis [43] predict production of a number of reactive species:

$$H_2O \rightarrow H_2,\ O_2,\ H_2O_2,\ OH,\ H,\ e^-_{aq},\ HO_2,\ O_2^-,\ HO_2^-,\ OH^-,\ H^+, \ldots$$

Since the lifetime of such species is very short, they are recombining fast and the pH of the irradiated water remains neutral. The real corrosion damage of cyclotron target entrance foils is caused by appearance of high local concentrations of reactive species on the foil surface, fast diffusion through protective film toward Havar® substrate and chemical interaction with the substrate. Thereby, the preliminary evaluation of the protective coating efficiency as diffusion barrier should be done before the direct test of few final coated Havar® entrance foils on a cyclotron facility. The most described in literature technique for diffusion barrier efficiency evaluation [31,44] was based on observation of copper atoms penetration through grain boundaries of metallic coatings at high temperatures. We propose two faster and easier tests using diffusion of protons of hydrochloric acid solution and gallium atoms through the inert protective film. Aluminum sputtered (2.5 μm) quartz samples $9 \times 9 \times 1$ mm (optical finishing) were used as substrates for protective coating deposition. Unlike aluminum, with its extreme susceptibility for both acid corrosion and liquid gallium corrosion, refractory metals like tantalum, zirconium, and niobium are chemically inert. Thus, the corrosion in the system aluminum covered with the inert coating can identify poor barrier properties of the protective coating (for more details see [45]).

The proton diffusion test was carried out by immersing the samples into 10% hydrochloric acid at 30 °C during 10 min. The hydrogen bubbles appeared on the surface of the coating reveal both macro porosity owing to macro particles generation during sputtering process and micro-voids and grain-boundaries depending on the coating microstructure. The results were evaluated due to the number of

hydrogen bubbles appeared on the surface of the coating. The acid test results were evaluated numerically in a scale from "1" to "5", where "1" meant the smallest amount of hydrogen bubbles and appropriately the best barrier quality of a coating.

The liquid gallium diffusion test was carried out by heating aluminated quartz samples coated with investigated alloy coatings (the same preparation of samples done in previous tests) with liquid gallium droplets during 40 h at 200 °C. Nb, Ta and Zr are inert for liquid Ga, while aluminum is well-known to be corroded extremely fast by liquid Ga causing the so called liquid–metal embrittlement. In the case of diffusion of gallium atoms through the film, they interacted with aluminum underlayer to form a liquid alloy and the protective film was ruined. That was what we had visually detected.

The velocity of penetration of liquid Ga through the film depends also on wettability. Wettability is the ability of a liquid to maintain the contact with a solid surface, resulting from intermolecular interactions when the two are brought together, and the force balance between the adhesive energy of the surface and the cohesive energy of the liquid determines it. High wettability corresponds to a low contact angle of a droplet and low wettability corresponds to a high contact angle respectively.

2.3. Microstructure analysis

The microstructures of the alloy thin films onto 9 × 9 × 1 mm amorphous quartz substrates were characterized by X-ray diffraction measurement in Panalytical (ex-Philips) PW3040/60 Diffractometer with 1.54 Å Cu Kα X-ray. The XRD investigation was carried out by performing the θ–θ Gonio scan in Bragg–Brentano configuration with 2θ from 10° to 100°. The XRD pattern of not covered quartz substrates had no any peaks because of a fully amorphous structure of the substrate. That is why the XRD patterns of investigated coatings had no additional peaks related to the substrate.

X'Pert Highscore software was used for fitting in order to obtain the peak position and the integral breadth. The average crystallite size D for the most intense peak was determined using the Debye–Scherrer formula.

Composition of the sputtered alloys has been determined by the energy dispersive X-ray spectroscope (EDX) coupled with the Scanning Electron Microscope Vega 3 XM (TESCAN). The same Scanning Electron Microscope Vega 3 XM (TESCAN) was used to observe the cross-sections of sputtered coatings.

3. Results

3.1. Nb–Zr alloy sputtering

The XRD patterns of 10 co-sputtered Nb–Zr alloy coatings of different composition deposited at $8{\cdot}10^{-3}$ mbar Ar pressure are shown in Fig. 2. In the case of maximum niobium content, several crystalline diffraction peaks were detectable, and the strongest peak was identified as (1 1 0)-line of bcc-Nb. The most intense peak in the XRD patterns corresponding to Nb(1 1 0) was shifted toward the lower angles with increasing zirconium content until it attained the position corresponding to bcc-Zr(1 1 0). Alloying 50% atomic zirconium and 50% atomic niobium leads to a broadening of (1 1 0) diffraction peak but the crystallite size D_{110} calculated according to the Debye–Scherrer formula (see Table 1) did not reach the critical value of 2.5 nm used for discrimination of amorphous and crystalline structure [46].

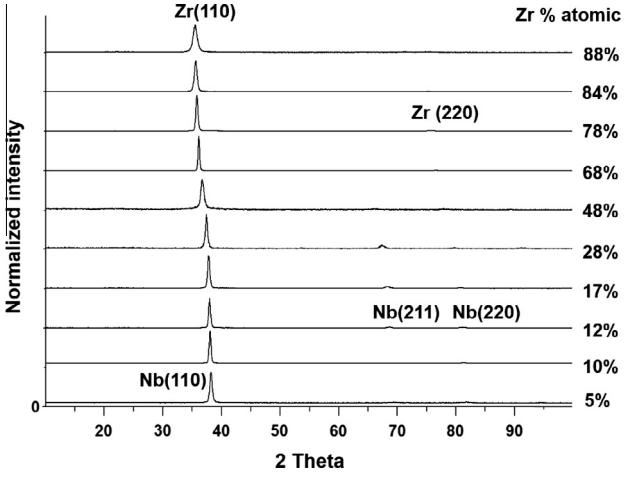

Fig. 2. XRD spectrums of Nb–Zr alloys of different composition.

The most intense peak position was used to estimate the content of each metal in alloy according to the Vergard's law. Vegard's law says that a linear relation exists between the Crystal Lattice Parameter a and the concentrations of the constituent elements at constant temperature.

According to the Vegard's rule for $Nb_{1-x}Zr_x$ alloy the relation connecting Cubic Lattice Parameter of alloy a_{NbZr} with Cubic Lattice Parameters of single metals a_{Nb} and a_{Zr} can be presented:

$$a_{NbZr} = (1 - x) \cdot a_{Nb} + x \cdot a_{Zr} \quad (1)$$

Single metal niobium and zirconium films were sputtered at the same pressure, current, on the same sample holder and during the same time as Nb–Zr alloy films. The XRD patterns of single metal films were analyzed and the Cubic Lattice Parameter (a_{110}) values were found to be a_{Nb} = 3.314 Å and a_{Zr} = 3.614 Å respectively. Thus, the content of zirconium x in Nb–Zr alloy was calculated, found from the linear equation:

$$a_{NbZr} = 3.314 + 0.3 \cdot x \quad (2)$$

Fig. 3 gives the graphic representation of the use of Vegard's rule for Nb–Zr sputtered alloys. The graph shows the line drawn through two points representing the Cubic Lattice Parameters for niobium and zirconium: a_{Nb} = 3.314 Å, a_{Zr} = 3.614 Å. When the Cubic Lattice Parameter for Nb–Zr alloy is postponed on Y-axis the X coordinate of the point on the line corresponds to the atomic percentage of zirconium.

Table 1 summarizes the most important parameters representing the correlation between the microstructure and the barrier properties of Nb–Zr alloy coatings. Nb–Zr alloys with higher zirconium content were found more resistant to the acid solution than Nb-rich alloys.

According to the acid test Nb–Zr alloy films with more than 50% zirconium showed better resistance. All compositions of Nb–Zr alloys besides Nb–Zr 10 with maximum zirconium content showed resistance to liquid gallium droplets. All Nb–Zr coatings showed partial surface wettability by liquid gallium droplet (the contact angle > 90°).

3.2. Nb–Ta alloy sputtering

Table 2 shows the key parameters describing the content, microstructure and protective behavior of Nb–Ta alloy coatings sputtered at $7{\cdot}10^{-3}$ mbar. Similar to Nb–Zr alloy Nb–Ta alloy films with less niobium content showed better resistance to the acid test. All compositions of Nb–Ta alloys besides Nb–Ta 8 showed resistance to the liquid gallium penetration. The liquid gallium surface wettability of the Nb–Ta also seem to be in agreement with the crystallite size measured.

The XRD patterns of Nb–Ta alloy coatings are presented in Fig. 4. All Nb–Ta coatings were crystalline. The Ta(1 1 0) and Nb(1 1 0) peaks appear at the same 2Theta angle ~38–39°, therefore it is not possible to use the Vegard's law for the alloy content estimation. Both body centered cubic (bcc) α-Ta(1 1 0) and tetragonal β-Ta(2 0 0) peaks are present in XRD spectrums of Nb–Ta alloys with less than 13% atomic of niobium. The incorporation of higher amounts of niobium stabilizes the bcc structure. Increasing the niobium content in alloys > 13% atomic results in increasing the amount of (2 1 1) crystalline phase.

During magnetron sputtering deposition processes, bcc α-phase tantalum, hexagonal β-phase tantalum or mixed phase tantalum grow on different substrates depending on specific deposition conditions. Since sputtering is a non-equilibrium process, the metastable β-phase Ta [47] or mixed phase Ta is more common to be

Table 1
Nb–Zr alloy coatings.

Sample number	Nb–Zr 1	Nb–Zr 2	Nb–Zr 3	Nb–Zr 4	Nb–Zr 5	Nb–Zr 6	Nb–Zr 7	Nb–Zr 8	Nb–Zr 9	Nb–Zr 10
Zr atomic %	5	10	12	17	28	48	68	78	84	88
Film thickness (μm)	1.4	1.6	1.7	1.7	1.6	1.7	1.9	1.9	1.9	1.9
Deposition rate (nm/s)	0.4	0.4	0.5	0.5	0.4	0.5	0.5	0.5	0.5	0.5
D_{110} (nm)	19	26	22	21	19	12	33	22	16	10
a_{110} (Å)	3.330	3.344	3.351	3.365	3.398	3.459	3.516	3.547	3.566	3.576
Liquid Ga corrosion	Corroded	Resists	Resists	Resists	Resists	Resists	Resists	Resists	Resists	Resists
Liquid Ga contact angle	100	90	100	110	120	130	110	110	120	110
Acid test	4	3	4	4	3	2	2	2	2	2

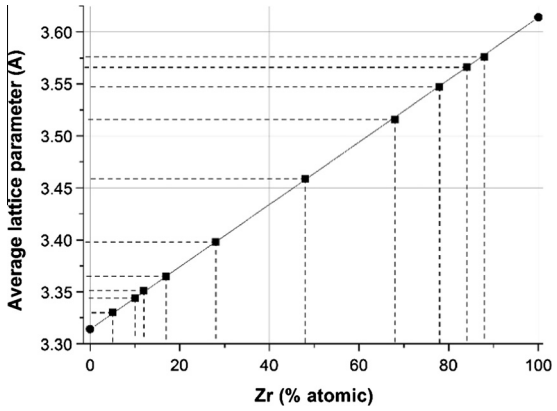

Fig. 3. Estimation of the content in Nb–Zr alloy according to the Vegard's law.

observed in sputter deposited thin films [48–51]. The β-to-α transition is promoted by heating up to 400 °C during deposition [52] or to 650–1000 °C after deposition [53,54]. The ion bombardment during deposition was shown to bring to different Ta phases dependent on the deposition system and bombarded ions kinetic energy and momentum [55–57]. The Ta phase formation was shown to depend also on sputtering gas [56], substrate [58,59], stress in the film [54], impurities level [60], deposition mechanics [61]. Even after a number of investigations focused on the influence of sputter deposition parameters, the mechanism of Ta phase growth is still unclear.

In a case of deposition of Nb–Ta alloy by sputtering the Ta phase formation is guided mostly by presence of Nb. Presence of Nb was shown to promote α-Ta phase formation [58,59], because Nb has the same bcc structure as α-Ta. For samples Nb–Ta 2 and Nb–Ta 3, which were placed on axis of one planar magnetron (where the plasma plum could touch the sample surface), other deposition factors have promoted β-Ta phase stabilization. These could be

(1) Electron bombardment by plasma plum is usually causing additional heating up to 250 °C. This temperature is not enough for β-to-α Ta phase transition and in a low vacuum conditions can promote oxidation by residual oxygen and stabilization of β-Ta phase [60];

(2) Ion bombardment by plasma plum could suppress α-Ta phase growth if the ion energy per deposited atom was low enough [57].

3.3. Ta–Zr alloy sputtering

The key parameters describing the content, microstructure and protective behavior of Ta–Zr alloy coatings sputtered at $8{\cdot}10^{-3}$ mbar are presented in Table 3. The XRD-patterns of sputtered Ta–Zr are presented in Fig. 5. According to the peak at 2Theta ~ 38°, that has the maximum intensity for all the alloys, the preferential orientation is (1 1 0). The full XRD spectrum of pure tantalum shows two crystalline peaks: (1 1 0) and (2 1 1) that signify the presence of bcc-Ta and absence of hcp-Ta phases. Substantial widening and intensity decrease of the (1 1 0) peak in the XRD spectrums of Ta–Zr alloy with zirconium atomic content from 30% to 70% signified formation of amorphous structure.

In order to prove the XRD results on alloys crystallinity Ta–Zr 2, Ta–Zr 6 and Ta–Zr 9 were deposited onto Si substrates following the same parameters as in previous deposition and the morphology of each film fracture was evaluated with SEM.

Fig. 6 shows the fracture surface of Ta–Zr 2 film with 96% atomic tantalum obtained with SEM. Clear columnar film morphology is observed. Fig. 8 shows the cross-sectional SEM micrograph of the fractured Ta–Zr 9 film with 88% atomic zirconium. Similar to Ta-rich film (Fig. 6) the morphology of Ta–Zr 9 is columnar but the size of the grains is significantly smaller.

Fig. 7 shows the cross-section of Ta–Zr 6 with 47% atomic Ta. The film has a boundary-free glass-like fracture surface morphology without observed grain boundaries.

Amorphous Ta–Zr alloy coatings showed superior resistance to both acid test and liquid gallium test. All Nb–Ta coatings similar to Nb–Zr showed incomplete surface wettability by liquid Ga. The contact angles of liquid gallium droplet on Nb–Ta coatings were bigger than those of Nb–Zr.

4. Discussion

4.1. Ability to form amorphous alloys

According to the empirical rules [62,63], the negative enthalpy of mixing and high radius mismatch of constituting elements are

Table 2
Nb–Ta alloy coatings.

Sample number	Nb–Ta 1	Nb–Ta 2	Nb–Ta 3	Nb–Ta 4	Nb–Ta 5	Nb–Ta 6	Nb–Ta 7	Nb–Ta 8	Nb–Ta 9	Nb–Ta 10
Ta atomic %	99	95	87	79	69	49	31	21	13	11
Film thickness (μm)	1.2	1.3	1.4	1.5	1.1	0.8	1.1	1.1	1.0	0.8
Deposition rate (nm/s)	0.3	0.4	0.4	0.4	0.3	0.2	0.3	0.3	0.3	0.2
D (nm)	20	44	38	10	12	7	10	11	11	9
Liquid Ga corrosion	Resists	Resists	Resists	Resists	Resists	Resists	Resists	Corroded	Resists	Resists
Liquid Ga contact angle	120	135	140	135	160	150	160	100	120	130
Acid test	3	1	1	2	4	5	5	5	2	5

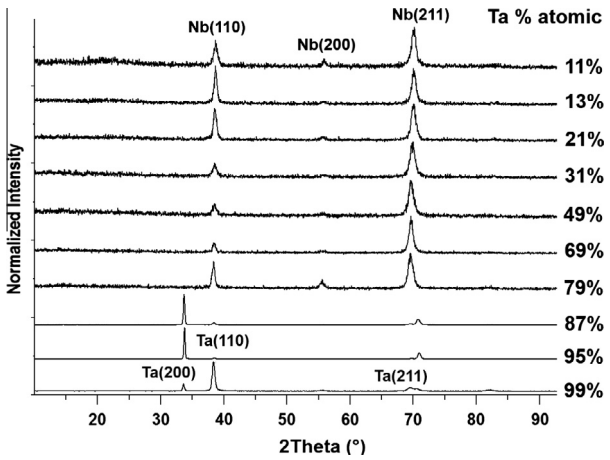

Fig. 4. XRD spectrums of Nb–Ta alloys.

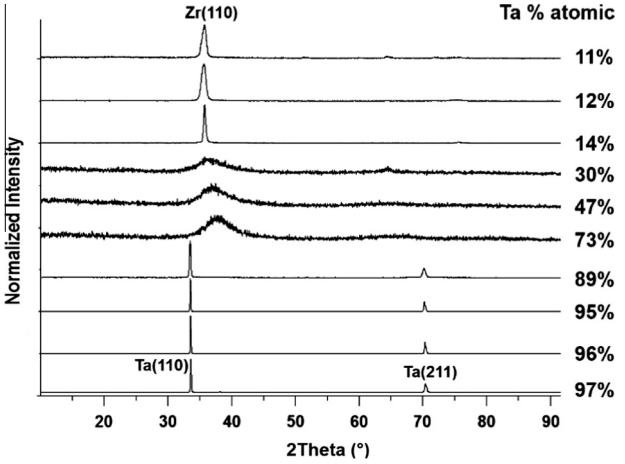

Fig. 5. XRD spectrums of Ta–Zr alloys.

known to favor the formation of amorphous phases. Since the enthalpies of formation of the solid solutions of Nb–Ta, Nb–Zr and Ta–Zr are positive and the difference of atomic radiuses is relatively small (R_{Nb} = 1.46 Å, R_{Ta} = 1.46 Å, R_{Zr} = 1.60 Å), all three binary alloy systems are not capable of amorphous structure forming. But the experimental results obtained in the current work and also by other authors have shown the formation of amorphous Ta–Zr alloys by co-sputtering [32] and co-condensation [30] in a range of compositions.

From the thermodynamic point of view the stability of any given phase is determined by its Gibbs free energy, with reference to the competing phases. Thus, an amorphous phase will be stable if its Gibbs free energy is lower than that of the competing crystalline phase in the glass-forming alloy systems. The Gibbs free energy of a system is defined as $G = H - TS$. In solid state the contribution to the Gibbs energy from entropy is much smaller than that from enthalpy, and therefore the entropy contribution to the free energy term can be neglected, and only the enthalpy term can be regarded as an indicator of the stability of an alloy [64].

In order to estimate the relative thermodynamic stability of the phases in investigated binary alloys, the enthalpy of formation of solid solution ΔH_{ss} and amorphous phase ΔH_{amorph} were calculated according to the advanced Miedema's model [65–67]. The results of calculation are presented in Figs. 9–11.

As it was mentioned above, the Gibbs free energy of the hypothetical amorphous phase ΔH_{amorph} should be lower than that of the competing crystalline phase ΔH_{ss} to provide the glass formation, so the value ($\Delta H_{amorph} - \Delta H_{ss}$) should be negative. The driving force for amorphous structure forming is the $-\Delta H_{amorph}$: the larger this value is, the easier is the glass formation. From the other side the resistance to crystallization is dependent on the difference in the Gibbs free energies of the amorphous and crystalline phases. The smaller this difference ($\Delta H_{amorph} - \Delta H_{ss}$) is, the higher is the stability of the amorphous phase [68]. Based on this, a γ^* parameter was proposed [69] as a measure of glass-forming ability (GFA) of alloy systems, defined as

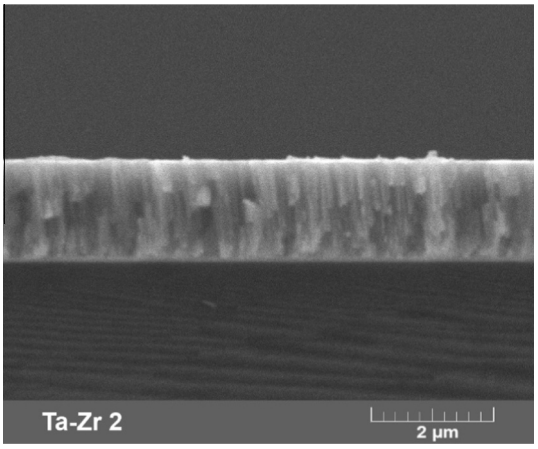

Fig. 6. Cross-sectional SEM micrograph of fractured Ta–Zr 2.

$$\gamma^* = \frac{-\Delta H_{amorph}}{\Delta H_{amorph} - \Delta H_{ss}} \quad (3)$$

The greater is the value of γ^* the higher is the stability of amorphous phase and so the glass-forming ability of the alloy is higher.

According to Fig. 9, the enthalpies of formation of the Nb–Ta solid solution are near zero values. The γ^* parameter is almost constant ~−1.003 for different alloy compositions. All these signify low capability of formation of amorphous alloy and low resistance to recrystallization. This hypothesis was correlated with experiment that did not show the presence of sputtered amorphous Nb–Ta alloys.

Table 3
Ta–Zr alloy coatings.

Sample number	Ta–Zr 1	Ta–Zr 2	Ta–Zr 3	Ta–Zr 4	Ta–Zr 5	Ta–Zr 6	Ta–Zr 7	Ta–Zr 8	Ta–Zr 9	Ta–Zr 10
Ta atomic %	97	96	95	89	73	47	30	14	12	11
Film thickness (µm)	1.3	1.7	1.9	1.4	1.4	1.3	1.0	1.3	1.1	1.2
Deposition rate (nm/s)	0.4	0.5	0.5	0.4	0.4	0.4	0.3	0.4	0.3	0.4
D_{110} (nm)	78	115	97	42	2	2	2	23	11	11
Liquid Ga corrosion	Resists	Resists	Resists	Resists	Resists	Resists	Resists	Resists	Resists	Resists
Liquid Ga contact angle	120	100	95	90	95	120	130	130	120	130
Acid test	1	2	1	2	1	1	1	2	1	5

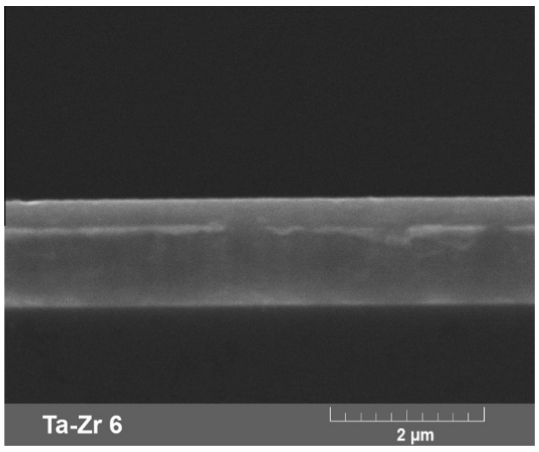

Fig. 7. Cross-sectional SEM micrograph of fractured Ta–Zr 6.

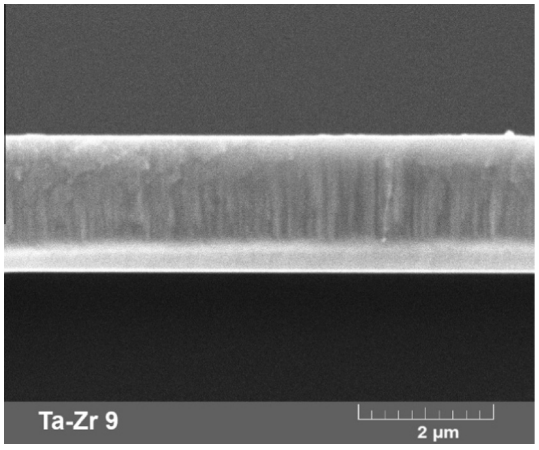

Fig. 8. Cross-sectional SEM micrograph of fractured Ta–Zr 9.

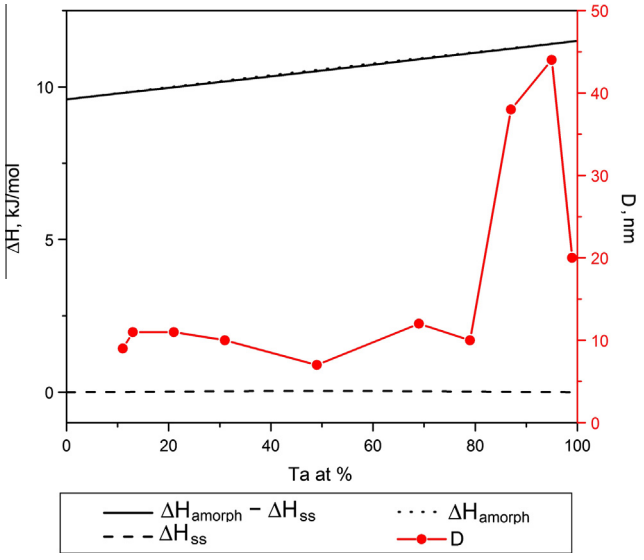

Fig. 9. Enthalpies of the Nb–Ta system calculated by Miedema's model.

Both Nb–Zr and Ta–Zr in the middle of the content range showed a region with $\Delta H_{amorph} - \Delta H_{ss} < 0$ (see Figs. 10 and 11). The driving force of the amorphous phase formation of these two

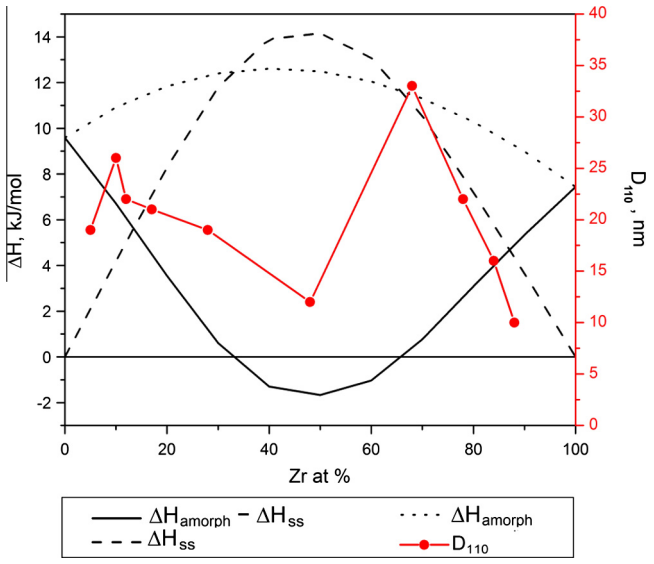

Fig. 10. Enthalpies of the Nb–Zr system calculated by Miedema's model.

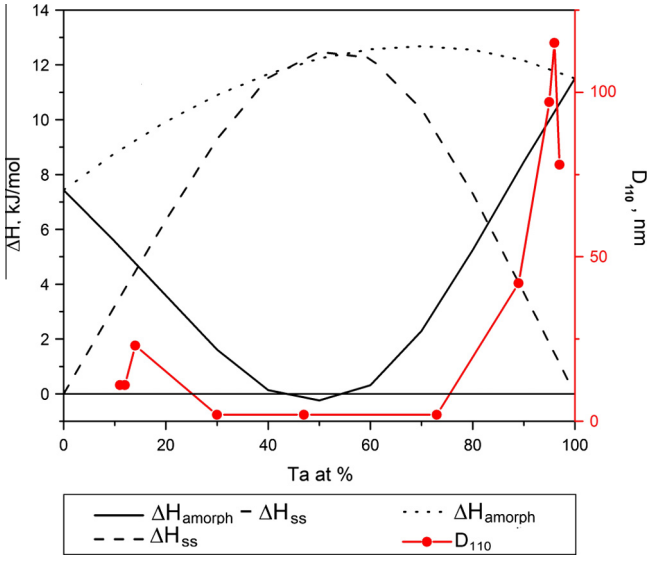

Fig. 11. Enthalpies of the Ta–Zr system calculated by Miedema's model.

alloys is similar $-\Delta H_{amorph} \sim 12$ kJ/mol. Nevertheless, amorphous Ta–Zr should have much higher resistance to recrystallization than Nb–Zr. It can be demonstrated also by calculation of the GFA parameter γ^* (see Table 4). Nb–Zr can have more wide amorphous forming phase composition range, but Ta–Zr present higher GFA parameter.

Such process as sputtering can course recrystallization of amorphous phase if the energy of atoms arriving to the substrate is enough. Possible recrystallization can explain the fact that we did not observe Nb–Zr amorphous alloys. Nevertheless formation of amorphous Nb–Zr has been reported by another technique as mechanical alloying [70] and IBM of multilayer thin films [37].

In order to correlate the proposed thermodynamic models with the experimental data on alloys amorphization ability the average crystallite size values D (nm) calculated from the XRD spectrums of corresponding binary alloys were added to the graphs (see Figs. 9–11).

Table 4
Calculated GFA of Nb–Zr and Ta–Zr alloys.

Zr atomic %	10	20	30	40	50	60	70	80	90
γ^*_{Nb-Zr}	−1.626	−3.334	−20.57	9.716	7.503	11.677	−14.69	−3.328	−1.682
γ^*_{Ta-Zr}	−1.437	−2.391	−29.61	−39.72	50.333	−84.02	−6.777	−2.767	−1.578

The Ta–Zr amorphous alloys were obtained in current work in a wider range of composition 30–73% atomic tantalum than was predicted by Miedema's model. Other authors also showed wider range of amorphous phase formation for Ta–Zr alloy [30,32]. It shows that for the sputtering process the thermodynamic model cannot describe the situation properly because kinetics plays the key role in the structure formation.

4.2. Diffusion barrier properties of binary alloy films

All the three coating systems Nb–Ta, Nb–Zr and Ta–Zr showed resistance to gallium atoms diffusion at investigated conditions. Small variations of liquid gallium droplet contact angles seem to be more attributed to the different grain size and, correspondingly, surface roughness rather than to gallium-coating chemical interaction.

The increase of the atomic percentage of niobium in Nb–Ta and Nb–Zr alloys showed the decreasing of the resistance to the acid test, it means, higher proton diffusion through the films. This phenomenon can be explained by a tendency of niobium-rich coatings to grow in a columnar microstructure with prolonged grain boundaries through the film, as pure niobium is famous about [71–73]. High affinity of niobium to oxygen promotes adsorption of oxygen and forming of niobium oxide in the grain boundaries [74] when sputtering is performed not in ultra-high vacuum, without preliminary degassing of all the system by plasma bombardment [75] and even exposure of pure sputtered niobium films to atmosphere was proven to induce oxidation along the grain boundaries [76]. Probably such oxidized grain boundaries can affect faster transport of the particles of the media through the film enlarging the distance between grains [74,77].

In general, Ta–Zr coatings showed higher resistance to acid proton diffusion than the other two systems Nb–Zr and Nb–Ta, that can be explained by the same high grain boundary oxidation in sputtered niobium.

5. Conclusions

The microstructure and diffusion barrier efficiency of co-sputtered Nb–Ta, Nb–Zr and Ta–Zr coatings were investigated. Co-sputtered Nb–Zr and Nb–Ta alloy coatings were found to be crystalline. Our test showed that the diffusion barrier efficiency of Nb–Zr and Nb–Ta decreased with the increase of Nb content.

Ta–Zr alloys showed to have higher amorphous phase forming ability during magnetron co-sputtering than Nb–Zr and Nb–Ta alloys. Dense amorphous Ta–Zr alloy coatings were obtained by co-sputtering in a range of composition with 30–73 at.% Ta. As far as sputtered amorphous Ta–Zr coatings showed superior diffusion barrier efficiency, amorphous $Ta_{55}Zr_{45}$ was chosen for deposition onto Havar® target foil for the irradiation test under the cyclotron accelerated proton beam.

Since amorphous Ta–Zr coatings showed also good resistance for gallium penetration, they can be suggested for protection from liquid metal corrosion, for example, for the high efficiency cyclotron targets cooled by liquid metals or liquid metal ^{85}Rb (m.p.: 39.3 °C) cyclotron targets for [^{82}Sr] production.

Acknowledgments

This work was financed by the V Group of INFN for Accelerator and Interdisciplinary Physics, with a contribution from BEST Cyclotrons.

We are thankful to prof. G. Fiorentini, Dr. G. Cuttone and Prof. M. Carpinelli, Dr. M. Bonardi for their precious support, all the staff of the INFN-LNL Service for Material Science and Technology applied to Nuclear Physics for their constant help and E. Tessarolo for critical reading and discussion.

References

[1] Cyclotron Produced Radionuclides: Operation and Maintenance of Gas and Liquid Targets, in: IAEA Radioisotopes and Radiopharmaceuticals Series, International Atomic Energy Agency, Vienna, 2012.
[2] D. Ferguson, P. Orr, J. Gillanders, G. Corrigan, C. Marshall, Measurement of long lived radioactive impurities retained in the disposable cassettes on the Tracerlab MX system during the production of [^{18}F]FDG, Appl. Radiat. Isot. 69 (2011) 1479–1485.
[3] J.S. Wilson, M.A. Avila-Rodriguez, R.R. Johnson, A. Zyuzin, S.A. McQuarrie, Niobium sputtered Havar foils for the high-power production of reactive [^{18}F]fluoride by proton irradiation of [^{18}O]H_2O targets, Appl. Radiat. Isot. 66 (2008) 565–570.
[4] K. Gagnon, J.S. Wilson, E. Sant, C.J. Backhouse, S.A. McQuarrie, Assessing the performance and longevity of Nb, Pt, Ta, Ti, Zr, and ZrO_2-sputtered Havar foils for the high-power production of reactive [^{18}F]F− by proton irradiation of [^{18}O]H_2O, Appl. Radiat. Isot. 69 (2011) 1330–1336.
[5] M.-A. Nicolet, Diffusion barriers in thin films, in: Thin Solid Films, Elsevier Sequoia S.A., Lausanne, 1978, pp. 415–443.
[6] M. Mehmood, E. Akiyama, H. Habazaki, A. Kawashima, K. Asami, K. Hashimoto, Effects of nanocrystalline heterogeneity on the corrosion behavior of sputter-deposited chromium–niobium alloys, Corros. Sci. 42 (2000) 361–382.
[7] K. Hashimoto, H. Habazaki, E. Akiyama, H. Yoshioka, J.H. Kim, P.Y. Park, A. Kawashima, K. Asami, Recent progress in corrosion-resistant new alloys prepared by sputter deposition., in: Scientific Report of Research Institute of Tohoku University A42, Institute for Materials Research of Tohoku University, Sendai, 1996, pp. 99–105.
[8] J. Bhattarai, X-ray photoelectron spectroscopic study on the anodic passivity of sputter-deposited W–Nb alloys in 12 M HCl solution, J. Sci. Res. 3 (2011) 457–470.
[9] H.-C. Kou, Y. Li, T.-B. Zhang, J. Li, J.-S. Li, Electrochemical corrosion properties of Zr- and Ti-based bulk metallic glasses, Trans. Nonferr. Met. Soc. China 21 (2011) 552–557.
[10] F.X. Qin, H.F. Zhang, Y.F. Deng, B.Z. Ding, Z.Q. Hu, Corrosion resistance of Zr-based bulk amorphous alloys containing Pd, J. Alloys Comp. 375 (2004) 318–323.
[11] B. Wang, X. Mei, H. Zhang, W. Hou, Y. Wang, Z. Wang, C. Dong, Resistance to He^{2+} induced irradiation damage in metallic glass $Zr_{64}Cu_{17.8}Ni_{10.7}Al_{7.5}$, J. Nucl. Mater. 444 (2014) 342–348.
[12] D.J. Magagnosc, G. Kumar, J. Schroers, P. Felfer, J.M. Cairney, D.S. Gianola, Effect of ion irradiation on tensile ductility, strength and fictive temperature in metallic glass nanowires, Acta Mater. 74 (2014) 165–182.
[13] M. Schütze, Corrosion Resistance of High-performance Materials: Titanium, Tantalum, Zirconium, Wiley, 2012.
[14] F.Y. Zhou, K.J. Qiu, H.F. Li, T. Huang, B.L. Wang, L. Li, Y.F. Zheng, Screening on binary Zr–1X (X = Ti, Nb, Mo, Cu, Au, Pd, Ag, Ru, Hf and Bi) alloys with good in vitro cytocompatibility and magnetic resonance imaging compatibility, Acta Biomater. 9 (2013) 9578–9587.
[15] Y. Tsutsumi, S. Yalatu, S. Migita, H. Doi, N. Nomura, K. Noda, T. Hanawa, Effect of alloying elements on corrosion behavior of Zr-based binary alloys in simulated body fluid, Meeting Abstracts, MA2012-02, 2012, 2136.
[16] T.R. Allen, R.J.M. Konings, A.T. Motta, 5.03 – Corrosion of zirconium alloys, in: R.J.M. Konings (Ed.), Comprehensive Nuclear Materials, Elsevier, Oxford, 2012, pp. 49–68.
[17] D. Turnbull, Metastable structures in metallurgy, Metall. Trans. B 12 (1981) 217–230.
[18] D.L. Zhang, T.B. Massalski, M.R. Paruchuri, Formation of metastable and equilibrium phases during mechanical alloying of Al and Mg powders, Metall. Mater. Trans. A 25 (1994) 73–79.
[19] M. Nastasi, F.W. Saris, L.S. Hung, J.W. Mayer, Stability of amorphous Cu/Ta and Cu/W alloys, J. Appl. Phys. 58 (1985) 3052–3058.

[20] J.H. Hsu, B.G. Alten, J.R. Childress, A. Gavrin, C.L. Chien, Structural and magnetic studies of metastable Gd–Cr alloys over the entire composition range, J. Appl. Phys. 70 (1991) 6308–6310.

[21] H.F. Rizzo, T.B. Massalski, A.W. Echeverria, Formation of metastable structures and amorphous phases in Pu-based systems using the sputtering technique, Metall. Trans. A 20 (1989) 813–823.

[22] K. Shimamura, Y. Matsumoto, T. Matsunaga, Some applications of amorphous alloy coatings by sputtering, Surf. Coat. Technol. 50 (1992) 127–133.

[23] J. Rivory, J.M. Frigerio, M. Harmelin, A. Quivy, Y. Calvayrac, J. Bigot, Preparation of Cu_xZr_{1-x} metallic glasses by sputtering and their thermal stability, electrical and optical properties, Thin Solid Films 89 (1982) 323–327.

[24] K. Bhanumurthy, G.K. Dey, S. Banerjee, Metallic glass formation by solid state reaction in bulk zirconium–copper diffusion couples, Scr. Metall. 22 (1988) 1395–1398.

[25] R.J. Highmore, A.L. Greer, Eutectics and the formation of amorphous alloys, Nature 339 (1989) 363–365.

[26] S.B. Newcomb, K.N. Tu, Transmission electron microscopic observations of amorphous NiZr alloy formation by solid-state reaction, Appl. Phys. Lett. 48 (1986) 1436–1438.

[27] C.J. Chen, J.C. Huang, H.S. Chou, Y.H. Lai, L.W. Chang, X.H. Du, J.P. Chu, T.G. Nieh, On the amorphous and nanocrystalline Zr–Cu and Zr–Ti co-sputtered thin films, J. Alloys Comp. 483 (2009) 337–340.

[28] H.S. Chou, J.C. Huang, L.W. Chang, Mechanical properties of ZrCuTi thin film metallic glass with high content of immiscible tantalum, Surf. Coat. Technol. 205 (2010) 587–590.

[29] O. Jin, B.X. Liu, Chemical and interface effects on glass forming ability under ion mixing in Zr–Ta system of positive heat of formation, J. Non-Cryst. Solids 211 (1997) 180–186.

[30] H. Hecht, G. Weigang, S. Eickert, U. Geyer, Formation area of thin amorphous Zr–Mn and Zr–Ta films prepared by cocondensation, Zeitsch. Phys. B Condens. Matter 100 (1996) 47–51.

[31] C. Li, J.H. Hsieh, Z.Z. Tang, Study on the amorphous Ta–Zr films as diffusion barrier in Cu metallization, J. Vac. Sci. Technol., A 26 (2008) 980–984.

[32] Z.Z. Tang, J.H. Hsieh, S.Y. Zhang, C. Li, Y.Q. Fu, Phase transition and microstructure change in Ta–Zr alloy films by co-sputtering, Surf. Coat. Technol. 198 (2005) 110–113.

[33] X.-X. Ma, G.-W. Guo, G.-Z. Tang, M.-R. Sun, L.-Q. Wang, Microstructure and properties of Nb/Ta multilayer films irradiated by a high current pulse electron beam, Chin. Phys. B 22 (2013) 056202.

[34] A. Cavalleri, F. Giacomozzi, L. Guzman, P.M. Ossi, Structure and superconductivity of Nb–Zr thin films, J. Phys.: Condens. Matter 1 (1989) 6685.

[35] A. Cavalleri, M. Dapor, F. Giacomozzi, L. Guzman, P.M. Ossi, M. Scotoni, Superconductivity in crystalline and amorphous Nb–Zr thin films, Mater. Sci. Eng. 99 (1988) 201–205.

[36] O. Jin, Z.J. Zhang, B.X. Liu, Alloying behavior induced by ion mixing in a system with positive heat of formation, J. Appl. Phys. 78 (1995) 149–154.

[37] T.L. Wang, S.H. Liang, J.H. Li, K.P. Tai, B.X. Liu, Abnormal alloying behaviour observed in an immiscible Zr–Nb system, J. Phys. D: Appl. Phys. 41 (2008) 095310.

[38] N. Savvides, B. Window, Unbalanced magnetron ion-assisted deposition and property modification of thin films, J. Vac. Sci. Technol., A 4 (1986) 504–508.

[39] C.A. Schuh, T.C. Hufnagel, U. Ramamurty, Mechanical behavior of amorphous alloys, Acta Mater. 55 (2007) 4067–4109.

[40] H. Chen, Y. He, G.J. Shiflet, S.J. Poon, Deformation-induced nanocrystal formation in shear bands of amorphous alloys, Nature 367 (1994) 541–543.

[41] W.H. Jiang, M. Atzmon, The effect of compression and tension on shear-band structure and nanocrystallization in amorphous $Al_{90}Fe_5Gd_5$: a high-resolution transmission electron microscopy study, Acta Mater. 51 (2003) 4095–4105.

[42] A. Entenberg, V. Lindberg, L. Fendrock, S.-K. Hong, T.S. Chen, R.S. Horwath, Dependence of stress on deposition conditions for sputtered copper films onto flexible polyimide substrates, in: K.L. Mittal, J.R. Susko (Eds.), Metallized Plastics 1, Springer, US, 1989, pp. 103–113.

[43] D.P. Butt, G.S. Kanner, L.L. Daemen, R.S. Lillard, In situ studies of aqueous corrosion of target and structural materials in water irradiated by an 800 meV proton beam., in: TMS Annual Meeting, Orlando, FL, 1997.

[44] S. Young-Hoon, S. Yukihiro, Diffusion barrier property of TiN and TiN/Al/TiN films deposited with FMCVD for Cu interconnection in ULSI, Sci. Technol. Adv. Mater. 5 (2004) 399.

[45] H. Skliarova, O. Azzolini, O. Cherenkova-Dousset, R.R. Johnson, V. Palmieri, Niobium-based sputtered thin films for corrosion protection of proton-irradiated liquid water targets for [^{18}F] production, J. Phys. D: Appl. Phys. 47 (2014) 045306.

[46] A. Regenbrecht, G. Minnigerode, K. Samwer, Formation region of amorphous thin CoZr and CuZr films prepared by cocondensation on hot substrates, Z. Phys. B: Condens. Matter 79 (1990) 25–31.

[47] Z. Cao, Q. She, Y. Huang, X. Meng, The rate sensitivity and plastic deformation of nanocrystalline tantalum films at nanoscale, Nanoscale Res. Lett. 6 (2011) 186.

[48] S.L. Lee, D. Windover, M. Audino, D.W. Matson, E.D. McClanahan, High-rate sputter deposited tantalum coating on steel for wear and erosion mitigation, Surf. Coat. Technol. 149 (2002) 62–69.

[49] S. Sato, Nucleation properties of magnetron-sputtered tantalum, Thin Solid Films 94 (1982) 321–329.

[50] S.L. Lee, D. Windover, T.M. Lu, M. Audino, In situ phase evolution study in magnetron sputtered tantalum thin films, Thin Solid Films 420–421 (2002) 287–294.

[51] A.A. Navid, A.M. Hodge, Controllable residual stresses in sputtered nanostructured alpha-tantalum, Scr. Mater. 63 (2010) 867–870.

[52] S. Masayuki, S. Satoko, S. Katsutaka, Y. Hideto, A. Yoshio, Preparation of low-resistivity α-Ta thin films on (001) Si by conventional DC magnetron sputtering, Jpn. J. Appl. Phys. 42 (2003) 4499.

[53] Y.M. Zhou, Z. Xie, H.N. Xiao, P.F. Hu, J. He, Effects of deposition parameters on tantalum films deposited by direct current magnetron sputtering, Vacuum 83 (2008) 286–291.

[54] L.A. Clevenger, A. Mutscheller, J.M.E. Harper, C. Cabral, K. Barmak, The relationship between deposition conditions, the beta to alpha phase transformation, and stress relaxation in tantalum thin films, J. Appl. Phys. 72 (1992) 4918–4924.

[55] P. Catania, R.A. Roy, J.J. Cuomo, Phase formation and microstructure changes in tantalum thin films induced by bias sputtering, J. Appl. Phys. 74 (1993) 1008–1014.

[56] D.W. Matson, E.D. McClanahan, S.L. Lee, D. Windover, Properties of thick sputtered Ta used for protective gun tube coatings, Surf. Coat. Technol. 146–147 (2001) 344–350.

[57] H. Ren, M. Sosnowski, Tantalum thin films deposited by ion assisted magnetron sputtering, Thin Solid Films 516 (2008) 1898–1905.

[58] D.W. Face, D.E. Prober, Nucleation of body-centered-cubic tantalum films with a thin niobium underlayer, J. Vac. Sci. Technol., A 5 (1987) 3408–3411.

[59] M. Stavrev, D. Fischer, F. Praessler, C. Wenzel, K. Drescher, Behavior of thin Ta-based films in the Cu/barrier/Si system, J. Vac. Sci. Technol., A 17 (1999) 993–1001.

[60] L. Liu, H. Gong, Y. Wang, J.P. Wang, A.T.S. Wee, R. Liu, Annealing effects of tantalum thin films sputtered on (001) silicon substrate, Mater. Sci. Eng., C 16 (2001) 85–89.

[61] S.L. Lee, J. Mueller, D. Windover, Real-time XRD characterization of growth of sputtered tantalum films, MRS Proc. 840 (2004).

[62] A. Inoue, H. Yamaguchi, T. Zhang, T. Masumoto, Al–La–Cu amorphous alloys with a wide supercooled liquid region, Mater. Trans. 31 (1990) 104–109.

[63] A. Inoue, T. Nakamura, N. Nishiyama, T. Masumoto, Mg–Cu–Y bulk amorphous alloys with high tensile strength produced by a high-pressure die casting method, Mater. Trans. 33 (1992) 937–945.

[64] C. Suryanarayana, A. Inoue, Bulk metallic glasses, CRC Press Taylor & Francisc Group, Boca Raton, 2011.

[65] R.F. Zhang, B.X. Liu, Proposed model for calculating the standard formation enthalpy of binary transition-metal systems, Appl. Phys. Lett. 81 (2002) 1219–1221.

[66] R.F. Zhang, B.X. Liu, Thermodynamic criterion for the formation of Laves phases in binary transition-metal systems, Philos. Mag. Lett. 85 (2005) 283–287.

[67] R.F. Zhang, S.H. Sheng, B.X. Liu, Predicting the formation enthalpies of binary intermetallic compounds, Chem. Phys. Lett. 442 (2007) 511–514.

[68] L.-C. Zhang, Thermodynamic approach for amorphous alloys from binary to multicomponent systems, in: D.J.C.M. Piraján (Ed.), Thermodynamics – Kinetics of Dynamic Systems, 2011.

[69] L. Xia, S.S. Fang, Q. Wang, Y.D. Dong, C.T. Liu, Thermodynamic modeling of glass formation in metallic glasses, Appl. Phys. Lett. 88 (2006) 171905.

[70] N. Al-Aqeeli, C. Suryanarayana, M.A. Hussein, Formation of an amorphous phase and its crystallization in the immiscible Nb–Zr system by mechanical alloying, J. Appl. Phys. 114 (2013) 153512–153516.

[71] C.T. Wu, Intrinsic stress of magnetron-sputtered niobium films, Thin Solid Films 64 (1979) 103–110.

[72] M.T. Tanvir, K. Fushimi, Y. Aoki, H. Habazaki, Oblique angle deposition of columnar niobium films for capacitor application, Mater. Trans. 49 (2008) 1320–1326.

[73] E. Bemporad, F. Carassiti, M. Sebastiani, G. Lanza, V. Palmieri, H. Padamsee, Superconducting and microstructural studies on sputtered niobium thin films for accelerating cavity applications, Supercond. Sci. Technol. 21 (2008) 125026.

[74] B.C. Okolo, Stress and microstructure of sputter deposited thin copper and niobium films, Universitätsbibliothek der Universität Stuttgart, Stuttgart, 2003.

[75] M.D. Malev, D.C. Weisser, Oxygen desorption during niobium sputtering for superconducting RF accelerators, Nucl. Instrum. Meth. Phys. Res., Sect. A 364 (1995) 409–415.

[76] J. Halbritter, Transport in superconducting niobium films for radio frequency applications, J. Appl. Phys. 97 (2005) 083904–083912.

[77] M. Murakami, T. Yogi, Strain in evaporated Nb thin films, J. Appl. Phys. 57 (1985) 211–215.